

RESEARCH ARTICLE

[View Article Online](#)
[View Journal](#) | [View Issue](#)



Cite this: *Mater. Chem. Front.*,
2024, 8, 3203

Tuning the organic ligands to optimize the nitrogen reduction performance of Co(II) or Ni(II)-based MOFs†

Ling Qin, ^{a,b} Ying-Xin Zhao,^a Qiang Liu,^a Jin-Long An,^a Han-Xi Wang,^a Mao-Feng Zhang, ^a Cheng-Wu Shi^a and He-Gen Zheng ^{*c}

The electrocatalytic nitrogen reduction to ammonia reaction (eNRR) can use clean energy and catalyst materials to convert N₂ to NH₃ under relatively mild conditions, but how to design and synthesize electrocatalysts has been the focus of eNRR research. Metal–organic frameworks (MOFs) are a class of crystalline porous materials with a high specific surface area, high porosity and a designable structure, and show great potential as new electrocatalysts. Designing and synthesizing MOFs with high stability and high conductivity, and optimizing the adsorption energy of MOFs with nitrogen and intermediates are the key to improve the electrocatalytic performance. Hence, five Co-MOFs with a similar structure were designed to investigate the effect of small changes in the organic ligand structure on nitrogen reduction performance. Among them, the Co-MOF based on the thiazole ligand shows the best eNRR performance, with the highest NH₃ yield (51.30 µg h⁻¹ mg_{cat}⁻¹) and Faraday efficiency (29.2%) at -0.4 V vs. RHE. This study can provide theoretical guidance for the design and development of high-performance eNRR electrocatalysts in the future.

Received 21st May 2024,
Accepted 2nd July 2024

DOI: 10.1039/d4qm00418c

rsc.li/frontiers-materials

1. Introduction

Ammonia (NH₃) is an indispensable chemical and one of the most important raw materials in modern agriculture and industry, and also has a large hydrogen capacity and high energy density, making it an ideal energy carrier.¹ The nitrogen content of the air is almost 80%, which has been the best raw material for industrial NH₃ synthesis.² Currently, the dominant process for NH₃ synthesis by nitrogen reduction is the old Haber–Bosch method, and the process requires high temperature and pressure conditions, consumes high energy and involves high risk during the reaction process.³ Therefore, it is necessary to develop a practical method that can perform the nitrogen reduction reaction for NH₃ synthesis at ambient temperature and pressure. The electrocatalytic nitrogen

reduction reaction (eNRR) offers potential for synthesis of NH₃ at ambient temperature and pressure. However, the activation and dissociation of N≡N and the competitive hydrogénolysis reaction (HER) are two major challenges for the eNRR.⁴

Metal–organic frameworks (MOFs) are a class of ordered structures assembled by metal nodes (or cluster units) and organic ligands *via* coordination bonds.^{5–7} They have the advantages of unique porous structure, diversity and adjustability of structure and composition, and have been widely used in gas separation, energy storage, drug transportation, catalysis and other fields.⁸ The use of highly active primary MOFs as catalysts is beneficial to improve the energy efficiency of the relevant reaction processes.^{9–12} Considering the uniqueness and diversity of MOF structures, the electrocatalytic activity of the primary MOFs can be improved by engineering such as adjusting the organic ligand and coordination structure and optimizing the electronic structure or constructing defects. Among them, the organic ligands of MOFs are important for electron trapping,¹³ separation and transport due to their induced and conjugated roles in organic structures. Heteroatoms (O, N, or S) with lone pair electrons are introduced into conjugated rings, thereby changing the electron density, forming an uneven electron density distribution and promoting the separation and transfer of charge.^{14,15} Chen *et al.*¹⁶ designed and prepared a series of Zr-MOF photocatalysts using organic ligands with different electron density distributions. The ligand

^a School of Chemistry and Chemical Engineering, Hefei University of Technology, Hefei, 230009, Anhui, P. R. China. E-mail: qinling@hfut.edu.cn

^b School of Materials Science and Engineering, Hefei University of Technology, Hefei, 230009, Anhui, P. R. China

^c State Key Laboratory of Coordination Chemistry, School of Chemistry and Chemical Engineering, Collaborative Innovation Center of Advanced Microstructures, Nanjing University, Nanjing 210023, P. R. China.

E-mail: zhenghg@nju.edu.cn

† Electronic supplementary information (ESI) available. CCDC 2350963 and 2350964. For ESI and crystallographic data in CIF or other electronic format see DOI: <https://doi.org/10.1039/d4qm00418c>



Scheme 1 The synthesis scheme of five Co-MOFs.

containing more N has the highest charge density difference, and has a significant effect on the optical properties of the catalyst. Here, we provide an effective strategy of modulating the microenvironment of the MOF catalysts by controlling the type of ligand to enhance their intrinsic activity.

In this work, five linear pyridine ligands with different functional blocks were designed, dpt, bptz, bpat, dpb and pds (dpt = 2,5-di(pyridin-4-yl)-1,3,4-thiadiazole, bptz = 3,6-bis(4'-pyridyl)-1,2,4,5-tetrazine, bpat = 3,5-bis(pyridine-4-yl)-4-amino-1,2,4-triazole, dpb = 1,4-di(pyridin-4-yl)benzene, and pds = 4,4-bipyridyl disulfide) and self-assembled with cobalt nitrate ($\text{Co}(\text{NO}_3)_2 \cdot 6\text{H}_2\text{O}$) as well as a co-ligand thiophene dicarboxylic acid (H_2tdc = thiophene-2,5-dicarboxylic acid) to obtain five Co-MOFs, that are $\text{Co-dpt-H}_2\text{tdc}$, $\text{Co-bptz-H}_2\text{tdc}$, $\text{Co-bpat-H}_2\text{tdc}$, $\text{Co-dpb-H}_2\text{tdc}$, and $\text{Co-pds-H}_2\text{tdc}$ (Scheme 1). The effect of different organic ligands on the performance of catalysts for the eNRR was explored. Among them, $\text{Co-dpt-H}_2\text{tdc}$ has the best nitrogen reduction properties and the highest NH_3 yield ($51.30 \mu\text{g h}^{-1} \text{ mg}_{\text{cat}}^{-1}$) and Faraday efficiency (29.2%) were obtained at -0.4 V vs. RHE . This work provides an effective strategy to improve electrochemical nitrogen reduction performance by modulating organic ligands.

2. Experimental

2.1 Preparation of $\text{Co-dpt-H}_2\text{tdc}$

0.02 g $\text{Co}(\text{NO}_3)_2 \cdot 6\text{H}_2\text{O}$, 0.005 g dpt and 0.004 g H_2tdc were dissolved in 2.5 mL N,N -dimethylformamide (DMF = N,N -dimethylformamide). To the mixture, 3 mL deionized water was slowly added and sonicated for 10 minutes. The mixed solution is placed in a stainless steel reactor lined with PTFE, after 2880 min at 85°C , cooled naturally to room temperature. Abundant red and prismatic crystals were obtained, the crystals were filtered, washed twice with DMF, deionized water and ethanol and dried, and the resulting crystal is $\text{Co-dpt-H}_2\text{tdc}$. The yield based on the dpt ligand was calculated to be 69%. The synthesis conditions and crystal information of five Co-MOFs are presented in Table S1 (ESI†).

2.2 Preparation of $\text{Co-bptz-H}_2\text{tdc}$

$\text{Co-bptz-H}_2\text{tdc}$ was synthesized in a similar way to $\text{Co-dpt-H}_2\text{tdc}$ except that dpt was replaced by bptz, and the ratio of DMF to water is adjusted to 1 mL:1 mL. The red and prismatic crystals were obtained. The yield based on the bptz ligand was calculated to be 51%.

2.3 Preparation of $\text{Co-bpat-H}_2\text{tdc}$

0.04 g $\text{Co}(\text{NO}_3)_2 \cdot 6\text{H}_2\text{O}$, 0.01 g bpat and 0.008 g H_2tdc were dissolved in 1 mL N,N -dimethylacetamide (DMA = N,N -dimethylacetamide), and to the mixture 1 mL deionized water was slowly added and sonicated for 10 minutes. The subsequent steps are similar to those for $\text{Co-dpt-H}_2\text{tdc}$. Purplish-red and prismatic crystals were obtained. The yield based on the bpat ligand was calculated to be 66%.

2.4 Preparation of $\text{Co-dpb-H}_2\text{tdc}$

0.02 g $\text{Co}(\text{NO}_3)_2 \cdot 6\text{H}_2\text{O}$, 0.005 g dpb and 0.01 g H_2tdc were dissolved in 1.5 mL DMF, and to the mixture 1 mL deionized water was slowly added and sonicated for 10 minutes. The subsequent steps are similar to those for $\text{Co-dpt-H}_2\text{tdc}$. Pink and needlelike crystals were obtained. The yield based on the dpb ligand was calculated to be 46%.

2.5 Preparation of $\text{Co-pds-H}_2\text{tdc}$

0.02 g $\text{Co}(\text{NO}_3)_2 \cdot 6\text{H}_2\text{O}$, 0.01 g pds and 0.008 g H_2tdc were dissolved in 2 mL DMF, and 1 mL deionized water was slowly added and sonicated for 10 minutes. The subsequent steps are similar to those for $\text{Co-dpt-H}_2\text{tdc}$. Pink and block crystals were obtained. The yield based on the pds ligand was calculated to be 63%.

3. Results and discussion

3.1 Characterization

3.1.1 Single crystal diffraction structure analysis of $\text{Co-dpt-H}_2\text{tdc}$, $\text{Co-bpat-H}_2\text{tdc}$, $\text{Co-dpb-H}_2\text{tdc}$ and $\text{Co-pds-H}_2\text{tdc}$. The crystal data and structures of $\text{Co-dpt-H}_2\text{tdc}$ (2269368) and $\text{Co-pds-H}_2\text{tdc}$ (2269367) have been reported in our previous literature.¹⁷ The structural formula of $\text{Co-dpt-H}_2\text{tdc}$ is $\{\text{Co}_2(\text{dpt})_2(\text{tdc})_2\}_n$, which belongs to the monoclinic crystal system of the $P2_1/c$ space group. In the least asymmetric unit, there are two $\text{Co}^{(II)}$ ions, two tdc^{2-} anions and two dpt ligands (Fig. 1a). Co1 and Co2 were connected by two N atoms from dpt in the axial position, and four O atoms from tdc^{2-} ligands in the plane position. Co1 and Co2 were linked by two carboxyl groups to form a binuclear cluster unit, which was connected by dpt and tdc^{2-} ligands to generate a three-dimensional structure (Fig. 1b). The binuclear cluster units can be regarded as 4-connected nodes, and dpt and tdc^{2-} ligands can be regarded as linkers. A topology analysis reveals that the

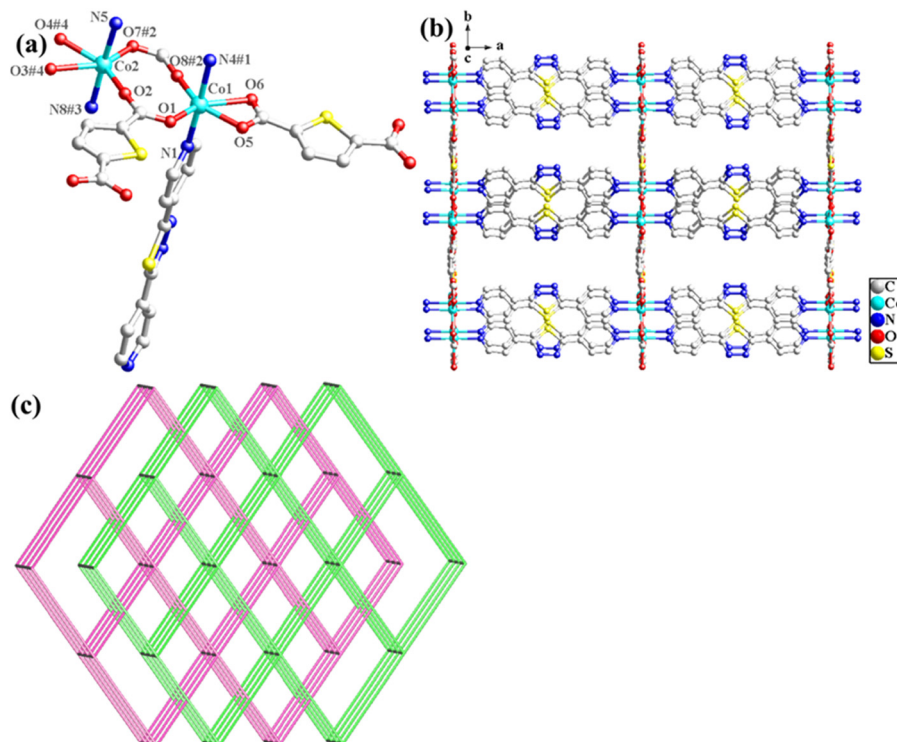


Fig. 1 (a) Coordination environment of Co(II) ions of Co-dpt-H₂tdc, symmetry code: #1 = 1 + x, y, z; #2 = x, 1/2 - y, -1/2 + z; #3 = -1 + x, y, z; #4 = x, 3/2 - y, -1/2 + z; (b) three-dimensional structure diagram of Co-dpt-H₂tdc; and (c) 2-fold interpenetrating **pcu** topology of Co-dpt-H₂tdc.

structure can be represented as a **pcu** topology, with the Schläfli symbol $\{4^{12}.6^3\}$ (Fig. 1c). The potential voids are large enough to be filled *via* mutual interpenetration of an independent equivalent framework, generating a 2-fold interpenetrating architecture. Table S2 (ESI[†]) shows the crystallographic data

and structure refinement details. Table S3 (ESI[†]) shows selected bond lengths and angles.

The structural formula of Co-bpat-H₂tdc is $\{[\text{Co}(\text{bpat})(\text{tdc})(\text{H}_2\text{O})\text{-DMA}]_n\}$, which belongs to the hexagonal crystal system of the $P\bar{6}_1$ space group. In the least asymmetric unit, there are one Co(II) ion,

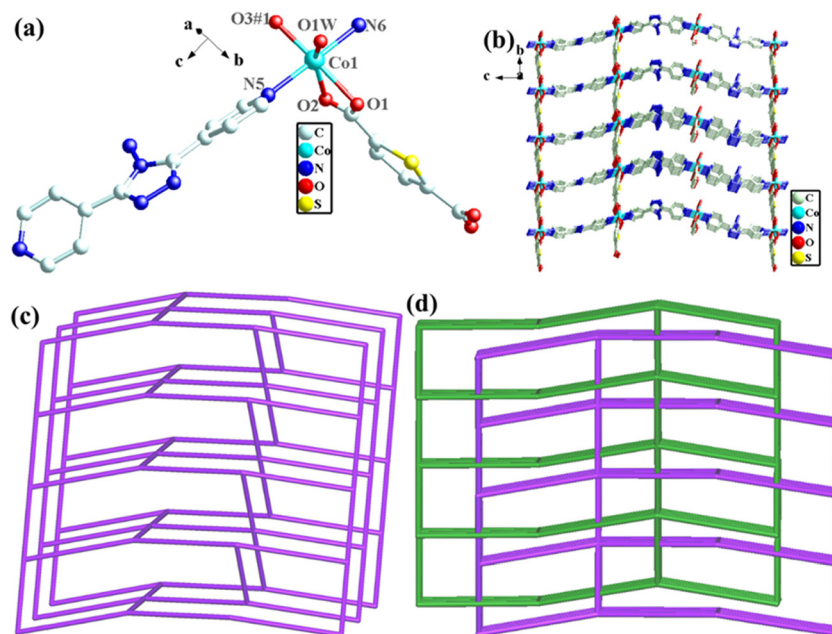


Fig. 2 (a) Coordination environment of Co(II) ions of Co-bpat-H₂tdc, symmetry code: #1 = x, -1 + y, z; (b) three-dimensional structure diagram of Co-bpat-H₂tdc; and (c) **quartz-dual** topology of Co-bpat-H₂tdc. (d) 2-fold interpenetrating **quartz-dual** net of Co-bpat-H₂tdc.

one tdc^{2-} anion, one bpat ligand, one coordinated H_2O and one lattice DMA (Fig. 2a). Co1 was connected by two N atoms from bpat in the axial position, three O atoms from tdc^{2-} ligands and one O atom from water molecule in the plane position. Relying on the coordinate interaction between nitrogen and Co ions, the bpat molecule bridges Co centers into a 6_1 helix (Fig. S1a, ESI[†]). The resulting 6_1 helices with the same handedness are further linked up by the tdc^{2-} ligands to form a chiral 3D framework (Fig. 2b). Attributed to the H-bond interaction between the coordinated H_2O and the amino group of bpat as well as the lattice DMA, the DMA molecules form a secondary helical chain inside the molecular helix (Fig. S1b, ESI[†]). Co1 can be regarded as 4-connected nodes, and bpat and tdc^{2-} ligands can be regarded as linkers. A topology analysis reveals that the structure can be represented as a **quartz-dual** topology, with the Schläfli symbol $\{4^{12}, 6^3\}$ (Fig. 1c), which is an intrinsically chiral net.^{18,19} The potential voids are large enough to be filled *via* mutual interpenetration of an independent equivalent framework, generating a 2-fold interpenetrating architecture.

The structural formula of Co-dpb-H₂tdc is $\{\text{Co}_2(\text{dpb})_2(\text{tdc})_2\}_n$, which belongs to the monoclinic crystal system of the $P2_1/c$ space group. Its structure is isomorphic to that of Co-dpt-H₂tdc. In the least asymmetric unit, there are two Co(II) ions, two tdc^{2-} anions and two dpb ligands (Fig. 3a). Co1 was five-coordinated and connected by two N atoms from dpb in the axial position, and three O atoms from tdc^{2-} ligands in the plane position. Co2 was six-coordinated by two N atoms from dpb in the axial position, and four O atoms from tdc^{2-} ligands in the plane position. Co1 and Co2 were linked by two carboxyl groups to form a binuclear cluster unit, which was connected by dpb and tdc^{2-} ligands to generate a three-dimensional structure. The binuclear cluster unit can be regarded as 4-connected nodes, and the dpb and tdc^{2-} ligands can be regarded as linkers. A topology analysis reveals that the structure can be represented as a **pcu** topology, with the Schläfli symbol $\{4^{12}, 6^3\}$ (Fig. 3b). The potential voids are large enough to be filled *via* mutual interpenetration of an independent equivalent framework, generating a 2-fold interpenetrating architecture (Fig. 3c).

The structural formula of Co-pds-H₂tdc is $\{\text{Co}_2(\text{pds})_2(\text{tdc})_2(\text{H}_2\text{O})\}_n$, which belongs to the orthorhombic crystal

system of the $C222_1$ space group. The least asymmetric unit contains two Co(II) ions, two pds ligands, two tdc^{2-} ligands, and one coordinated water molecule (Fig. 4a). Co1 and Co2 were linked by two carboxyl groups and one water molecule to form a binuclear cluster unit, which was connected by pds and tdc^{2-} ligands to generate a two-dimensional structure (Fig. 4b).

3.1.2 PXRD spectra and SEM of Co-dpt-H₂tdc, Co-bptz-H₂tdc, Co-bpat-H₂tdc, Co-dpb-H₂tdc, and Co-pds-H₂tdc. The standard powder X-ray diffraction (PXRD) spectra of Co-dpt-H₂tdc, Co-bpat-H₂tdc, Co-dpb-H₂tdc, and Co-pds-H₂tdc simulated from single crystal diffraction data matched well with the XRD spectra of the synthesized samples (Fig. 5 and Fig. S2a-c, ESI[†]), which confirmed the successful synthesis and high purity of the sample. The single crystal quality of Co-bptz-H₂tdc is not high, so its single crystal data were not analyzed. According to its cell data and powder diffraction pattern (Fig. S2d, ESI[†]), it is isomorphic to Co-dpt-H₂tdc. The above results confirmed that Co-dpt-H₂tdc, Co-bptz-H₂tdc, Co-bpat-H₂tdc, Co-dpb-H₂tdc, and Co-pds-H₂tdc were successfully synthesized. Scanning electron microscopy (SEM) was then used to characterize the morphology of Co-dpt-H₂tdc. As can be seen in Fig. 6a, Co-dpt-H₂tdc has a regular and uniform bulk shape. As shown in Fig. 6b, the elemental distribution map shows that the elements Co, C, N, O, and S are uniformly dispersed in Co-dpt-H₂tdc.

3.1.3 XPS spectra and SEM of Co-dpt-H₂tdc, Co-bptz-H₂tdc, Co-bpat-H₂tdc, Co-dpb-H₂tdc, and Co-pds-H₂tdc. Fig. 7a and Fig. S3a-S6a (ESI[†]) show the full XPS spectra of Co-dpt-H₂tdc, Co-bptz-H₂tdc, Co-bpat-H₂tdc, Co-dpb-H₂tdc, and Co-pds-H₂tdc. In addition to the H₂tdc co-ligand containing one S element, the dpt and pds ligands also contain one S element, therefore, the S content in Co-dpt-H₂tdc and Co-pds-H₂tdc is much higher than those in the other three Co-MOFs.²⁰ Besides, the highest N content appeared in Co-bpat-H₂tdc. These results are consistent with the proportion of heteroatoms in organic ligands. In the Co 2p XPS spectrum of Co-dpt-H₂tdc (Fig. 7b), the peaks located at 781.06 and 796.79 eV can be attributed to Co^{2+} $2p^{1/2}$ and $2p^{3/2}$, while the peaks located at 785.38 and 802.27 eV can be attributed to satellite peaks. In the C 1s XPS spectrum (Fig. 7c), the peaks located at 284.2, 285.0, 285.9, and 287.9 eV can be attributed to C-C, C-O, C-N/C-S, and O=C-O.

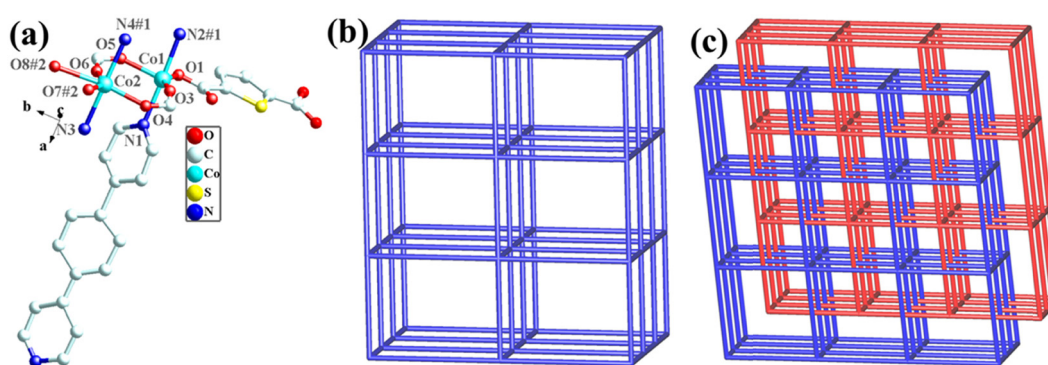


Fig. 3 (a) Coordination environment of Co(II) ions of Co-dpb-H₂tdc, symmetry code: #1 = $-1 + x, y, z$; #2 = $x, 3/2 - y, -1/2 + z$; (b) **pcu** topology of Co-dpb-H₂tdc; and (c) 2-fold interpenetrating **pcu** net of Co-dpb-H₂tdc.

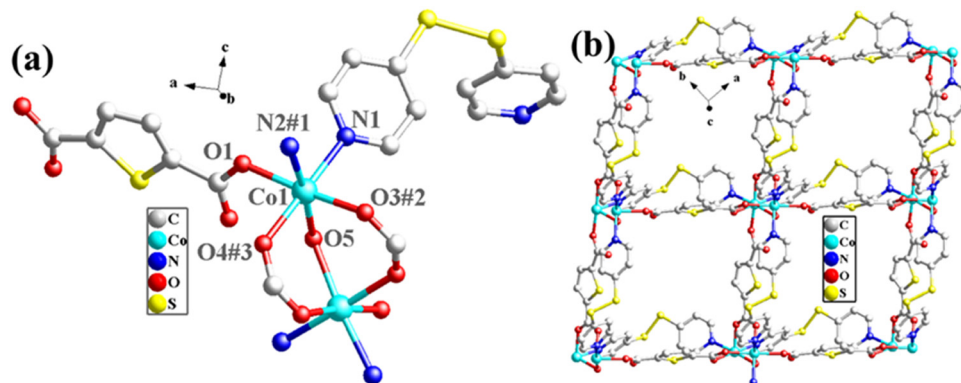


Fig. 4 (a) Coordination environment of Co(II) ions in Co-pds-H₂tdc, symmetry code: #1 = $1/2 + x, 1/2 + y, z$; #2 = $-1/2 + x, 1/2 + y, z$; #3 = $5/2 - x, 1/2 + y, 3/2 - z$; (b) two-dimensional structure diagram of Co-pds-H₂tdc.

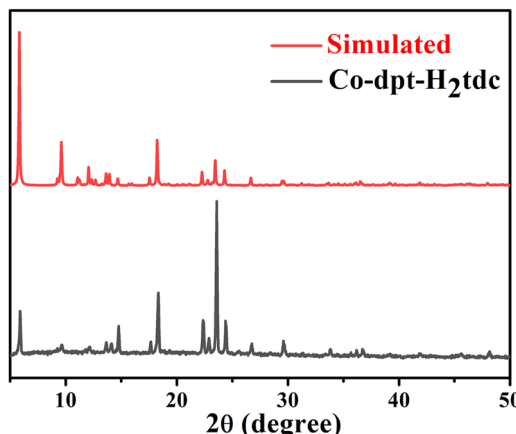


Fig. 5 PXRD pattern of synthesized Co-dpt-H₂tdc and standard spectra simulated using single crystal data.

In the N 1s XPS spectrum (Fig. 7d), the peaks located at 399.4, 399.9 and 401.4 eV can be attributed to Co-N, C-N and N-N.^{21,22} In the O 1s spectrum of the sample (Fig. 7e), the peaks observed at 530.98 and 532.08 eV can be attributed to Co-O and O=C-O, respectively.^{21,23} In the S 2p XPS spectrum (Fig. 7f), two peaks located at 163.86 and 164.84 eV can be attributed to C-S-C, the peak at 165.80 eV can be attributed to

C=S, and there were more C=S bonds in Co-dpt-H₂tdc compared to those in the other S 2p spectra. The new peaks at 401.4 eV in the N 1s XPS spectrum for Co-bpat-H₂tdc (Fig. S4c, ESI[†]) compared to that in Co-dpt-H₂tdc are attributed to the amino group. In addition, since the dpb and pds ligands of Co-dpb-H₂tdc and Co-pds-H₂tdc do not contain N-N, there were no N-N peaks in the N 1s XPS spectra (Fig. S5c and S6c, ESI[†]). In addition, since there is S-S in the pds ligand in Co-pds-H₂tdc (Fig. S6f, ESI[†]), in the S 2p XPS spectrum there is a S-S peak at 163.87 eV, instead of C=S in Co-dpt-H₂tdc. The bonding information from the XPS spectra is consistent with that obtained from single crystal diffraction data (Fig. S3–S6, ESI[†]).

3.2 Electrochemical NRR performance

To evaluate the ambient eNRR performance, catalysts were coated on a carbon cloth (CC) (2 cm × 1 cm) and tested in 0.1 M Na₂SO₄ solution under ambient conditions using a H-type electrolytic cell (Nafion 115 membrane for isolation). The carbon cloth supported by the catalyst is fixed in the cathode chamber through the platinum plate electrode clamp. The generated NH₃ was quantified by the indophenol blue method and Nessler's reagent spectrophotometry, and the content of the by-product hydrazine hydrate (N₂H₄) was also

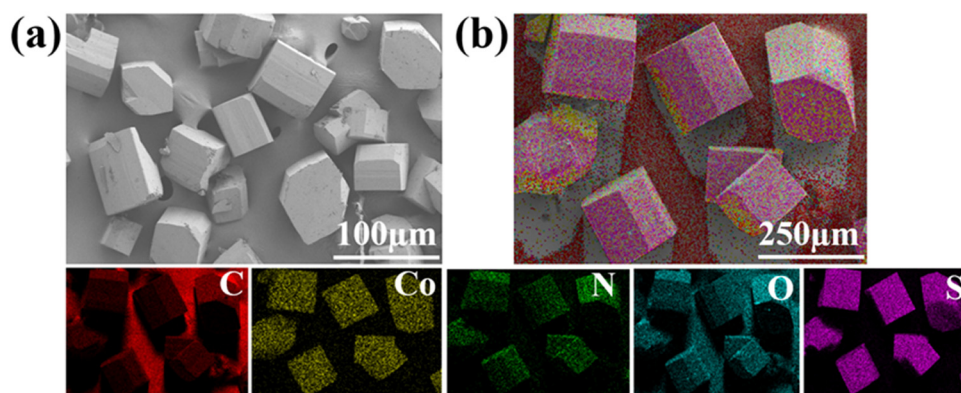


Fig. 6 (a) SEM and (b) EDS of Co-dpt-H₂tdc.

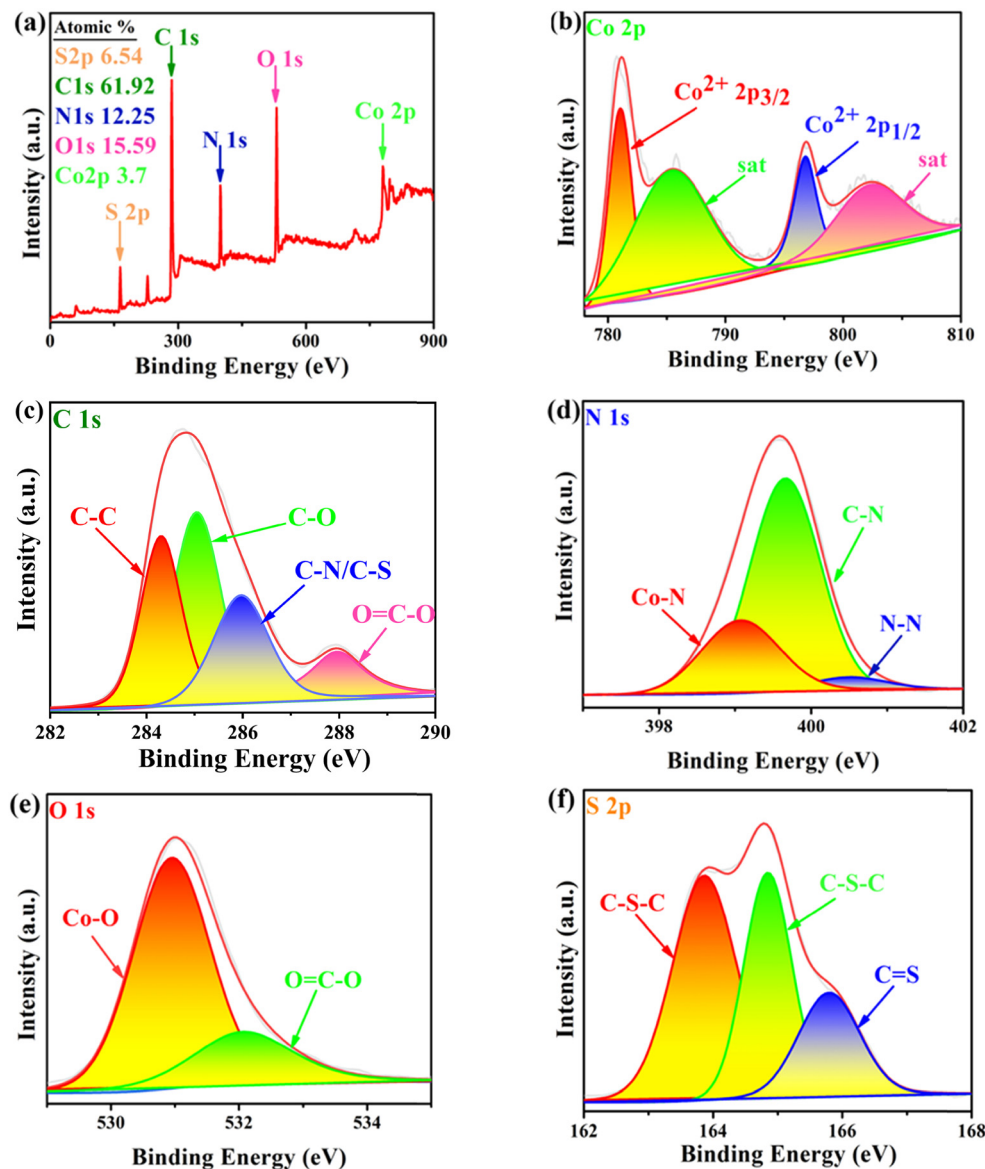


Fig. 7 (a) XPS full spectra of Co-dpt-H₂tdc; (b) Co 2p; (c) C 1s; (d) N 1s; (e) O 1s; and (f) S 2p.

tested using the Watt–Chrisp method to exclude interference from by-products. Fig. S7–S9 (ESI[†]) show the standard curves for the determination of NH₃ and N₂H₄.

The linear sweep voltammetry (LSV) curves of five Co-MOFs in Ar and N₂ saturated 0.1 M Na₂SO₄ electrolytes (Fig. 8a and Fig. S10a–S13a, ESI[†]) were obtained to evaluate the eNRR activity. For these Co-MOFs, the current densities in N₂ were higher than that in Ar at different potentials from −0.2 V to −0.7 V, the difference in current density is due to the consumption of electrons during the eNRR process, indicating that all five Co-MOFs show eNRR activity. In addition, the eNRR performance of five Co-MOFs was evaluated by means of the *i*–*t* method at different voltages, the *i*–*t* curve of Co-dpt-H₂tdc (Fig. 8b) shows that the current density remains stable from −0.2 V to −0.6 V, the NH₃ yield was calculated using the indophenol blue method and the UV-visible spectra at the

corresponding voltage are shown in Fig. 8c. As shown in Fig. 8d, the NH₃ yield as well as Faraday efficiency (FE) of Co-dpt-H₂tdc showed a volcano-like trend, with the best NH₃ yield (51.30 $\mu\text{g h}^{-1} \text{mg}_{\text{cat}}^{-1}$) and FE (29.2%) at −0.4 V. The *i*–*t* tests were performed on Co-bptz-H₂tdc at different potentials from −0.3 V to −0.7 V (Fig. S10b, ESI[†]), and the highest NH₃ yield (40.98 $\mu\text{g h}^{-1} \text{mg}_{\text{cat}}^{-1}$) and FE (67.4%) were obtained at −0.3 V (Fig. S10c and d, ESI[†]); the *i*–*t* test was performed at different potentials from −0.3 V to −0.7 V for Co-bpat-H₂tdc (Fig. S11b, ESI[†]), and the highest NH₃ yield (35.93 $\mu\text{g h}^{-1} \text{mg}_{\text{cat}}^{-1}$) and FE (17.4%) were obtained at −0.5 V (Fig. S11c and d, ESI[†]); the *i*–*t* test was performed at different potentials from −0.3 V to −0.7 V for Co-dpb-H₂tdc (Fig. S12b, ESI[†]), and the highest NH₃ yield (22.86 $\mu\text{g h}^{-1} \text{mg}_{\text{cat}}^{-1}$) and FE (25.9%) were achieved at −0.3 V (Fig. S12c and d, ESI[†]); the *i*–*t* test was performed at different potentials from −0.2 V to −0.6 V for Co-pds-H₂tdc

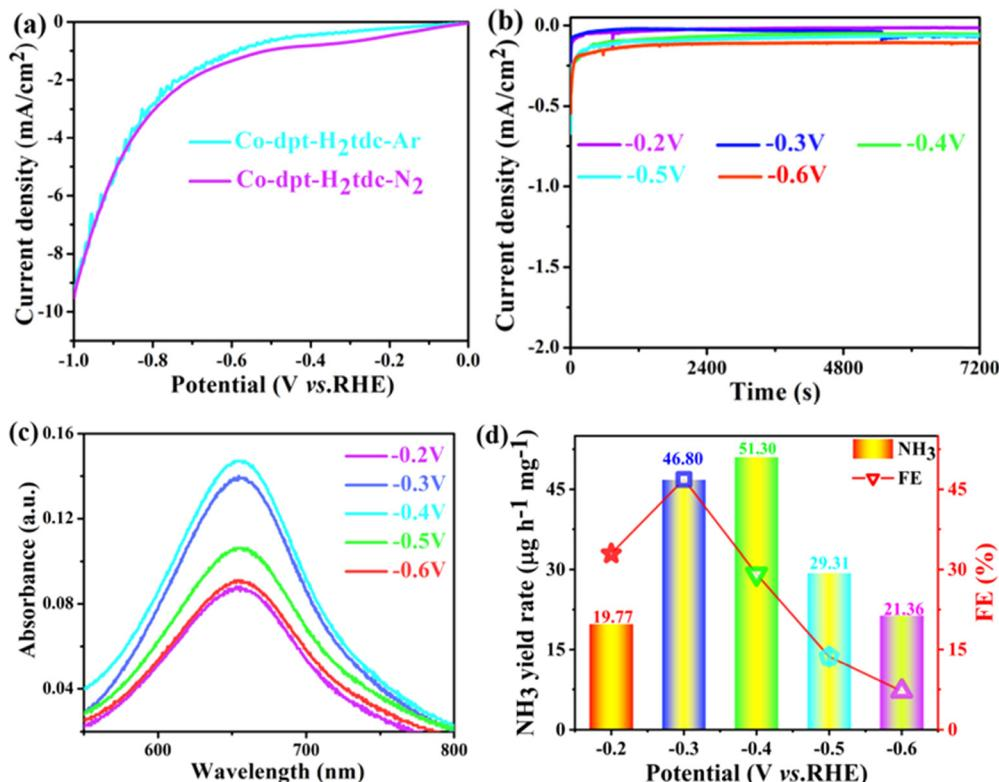


Fig. 8 (a) Polarization curves of Co-dpt-H₂tdc in N₂ and Ar-saturated 0.1 M Na₂SO₄ electrolyte; (b) time-dependent current densities curves of Co-dpt-H₂tdc at different potentials from -0.2 V to -0.6 V; (c) UV-vis spectra were estimated with the indophenol blue method at five given voltages for Co-dpt-H₂tdc; and (d) NH₃ yield and FE of Co-dpt-H₂tdc at different potentials from -0.2 V to -0.6 V.

(Fig. S13b, ESI[†]), and the highest NH₃ yield (19.75 $\mu\text{g h}^{-1} \text{mg}_{\text{cat}}^{-1}$) and FE (12.2%) were achieved at -0.3 V (Fig. S13c and d, ESI[†]). By comparing the NH₃ yields of the five Co-MOFs, the yields follow the following order: Co-dpt-H₂tdc > Co-bptz-H₂tdc > Co-bpat-H₂tdc > Co-dpb-H₂tdc > Co-pds-H₂tdc (Fig. S14, ESI[†]).

In order to elucidate the better eNRR activity of Co-dpt-H₂tdc compared to the other four catalysts, electrochemically active surface area (ECSA) tests were carried out to analyze the effect of active sites on the eNRR.^{24,25} Firstly, in the non-Faraday interval, the CV curves were measured at different scan rates for the five catalysts to obtain their double layer capacitance (C_{dl}) (Fig. S15, ESI[†]), the C_{dl} values of the five catalysts, Co-dpt-H₂tdc, Co-bptz-H₂tdc, Co-bpat-H₂tdc, Co-dpb-H₂tdc and Co-pds-H₂tdc, were 3.2193 mF cm⁻², 1.41075 mF cm⁻², 1.04568 mF cm⁻², 0.814 mF cm⁻², and 0.45343 mF cm⁻², respectively. The ECSA values for each catalyst were then determined according to the relationship ECSA = $C_{\text{dl}}/C_{\text{s}}$.²⁶ Co-dpt-H₂tdc has the largest electrochemical surface area, as shown in Fig. S15g (ESI[†]), the ECSA value of Co-dpt-H₂tdc was almost 7 times higher than that of Co-pds-H₂tdc, and the results suggest that Co-dpt-H₂tdc may provide more active sites for the eNRR reaction. Secondly, the charge transfer capacity of the five catalysts was also measured by electrochemical impedance spectroscopy (EIS) and Fig. S16 (ESI[†]) shows the EIS of the five catalysts. As shown in the Nyquist diagram, Co-dpt-H₂tdc has the lowest charge transfer resistance (R_{ct})

among the five catalysts, suggesting that Co-dpt-H₂tdc has the strongest electron-hole pair separation and charge transfer capacity. For Co-pds-H₂tdc, the non-conjugation pds ligand caused a poor conductivity compared to the other four catalysts. The introduction of heteroatoms N and S with lone pairs of electrons into conjugated ligands can modulate the charge transfer capacity of the organic ligand. Both the ECSA and EIS results are consistent with the eNRR results, which indicates that regulating the microenvironments of the catalysts by changing the ligand type and increasing the intrinsic activity of Co-MOFs is an effective strategy.

In order to exclude possible interference by pollutants, a series of controlled experiments were carried out (Fig. 9a). eNRR experiments on Co-dpt-H₂tdc were carried out at the open-circuit potentials with nitrogen as the feed gas, and the intensity of the UV-visible absorption peaks was comparable to that of the blank electrolyte, indicating that no NH₃ was produced at open-circuit potentials. Similar results were obtained when the bare carbon cloth was tested at -0.4 V with N₂ as a feed gas. In addition, when we change N₂ into Ar as a feed gas, the UV-visible absorption peak intensity is slightly higher than that of the blank electrolyte, but the intensity is much lower than that of Co-dpt-H₂tdc at -0.4 V with nitrogen as the feed gas, so the NH₃ yield under Ar conditions is negligible. The above results suggest that the observed NH₃ is mainly produced through the eNRR. The complex reaction pathway of the eNRR raises concerns about the possible

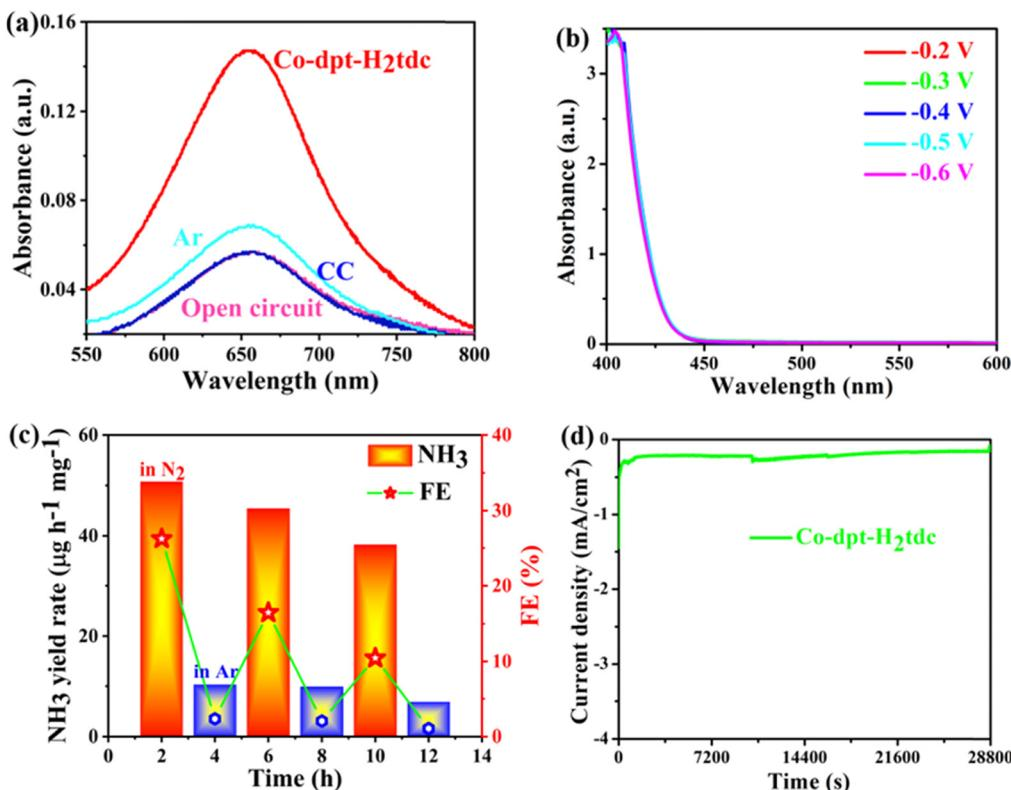


Fig. 9 (a) UV-visible absorption spectra of the electrolytes after electrolysis at -0.4 V for 2 h with Ar-saturated electrolyte (Ar), without Co-dpt-H₂tdc catalyst (CC), or at an open circuit (open circuit); (b) UV-vis absorption spectra of the electrolyte after N_2 electroreduction over Co-dpt-H₂tdc at a series of potentials from -0.2 V to -0.6 V for 2 h *via* the Watt and Chrissp method; (c) alternating cycle experiment in which Co-dpt-H₂tdc is sequentially electrolyzed for 2 h in N_2 and Ar saturated electrolytes at -0.4 V potential; and (d) current density–time curve of Co-dpt-H₂tdc electrolyzed in a N_2 saturated electrolyte for 8 h at -0.4 V.

formation of the byproduct N_2H_4 , the electrolyte was tested at different voltages of Co-dpt-H₂tdc and no absorbance was detected at 455 nm (Fig. 9b), indicating that byproduct N_2H_4 production during the eNRR is excluded, and it can be inferred that Co-dpt-H₂tdc exhibits excellent selectivity for the eNRR.

A long-term cycling test was further performed to investigate the stability property of the Co-dpt-H₂tdc electrocatalyst. The alternating cycling test of the electrocatalytic eNRR was performed at -0.4 V using N_2 and Ar saturated 0.1 M Na_2SO_4

(Fig. 9c). The NH_3 yield rate and Faradaic efficiency of the Co-dpt-H₂tdc catalyst can be maintained in each cycle in a N_2 -saturated electrolyte, while very low activity is observed in an Ar-saturated electrolyte, which indicates that NH_3 production was generated *via* N_2 electrochemical reduction.²⁷ More importantly, Co-dpt-H₂tdc exhibited great robustness and durability for a continuous 8 h long electrochemical NRR, with almost no decrease of the NH_3 yield rate and FE (Fig. 9d). In addition, the structural integrity of Co-dpt-H₂tdc electrocatalysts after 2 h of

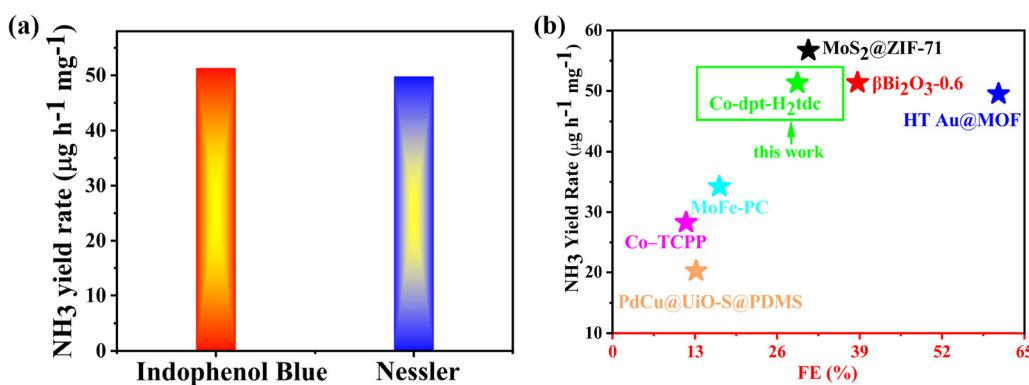


Fig. 10 (a) Comparison of the NH_3 yield for NH_3 of Co-dpt-H₂tdc at -0.4 V measured by Nessler's reagent spectrophotometry and indophenol blue spectrophotometry; (b) comparison of eNRR performances with those of some reported electrocatalysts.

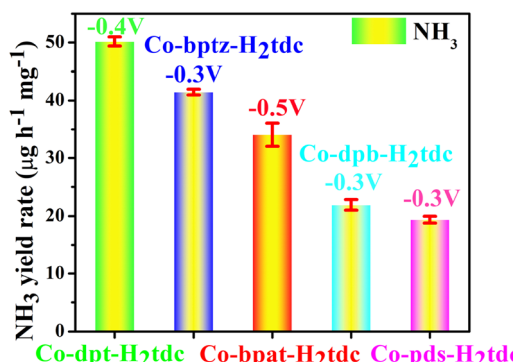


Fig. 11 NH₃ yield rate of five Co-MOF-based electrocatalysts based on similar ligands at their respective maximum potential.

eNRR testing was verified using PXRD patterns (Fig. S17, ESI[†]), which showed that the XRD pattern of Co-dpt-H₂tdc did not change after eNRR testing compared to the XRD spectra simulated from the single crystal data as well as the XRD pattern of Co-dpt-H₂tdc prior to eNRR testing.

We tested the ammonia yield rate of Co-dpt-H₂tdc at -0.4 V by Nessler's reagent spectrophotometry, and the NH₃ yield rate at -0.4 V determined by Nessler's reagent spectrophotometry approximates the results detected by the indophenol blue method (Fig. 10a). These results confirm the accuracy of our method for detecting ammonia yield. Furthermore, it is noteworthy that Co-dpt-H₂tdc exhibits very superior performance compared to other eNRR electrocatalysts (Fig. 10b and Table S4, ESI[†]).²⁸⁻³³

According to the above eNRR test results, the five Co-MOFs have different eNRR properties (Fig. 11), which confirmed that tuning the organic ligands can optimize the nitrogen reduction to ammonia performance of Co-MOFs.

To verify the above results, we synthesized five Ni-MOFs using the same ligand and the same method, namely, Ni-dpt-H₂tdc, Ni-bptz-H₂tdc, Ni-bpat-H₂tdc, Ni-dpb-H₂tdc, and Ni-pds-H₂tdc, and the standard powder diffraction spectra simulated from the single-crystal diffraction data matched well with the XRD spectra of the five Ni-MOFs (Fig. S18, ESI[†]), which confirmed the successful synthesis of the samples. The results of eNRR tests show that the sequence of the five Ni-MOFs is consistent with that of the Co-MOFs (Fig. S19, ESI[†]). The results show that it is an effective strategy to improve the performance of electrocatalytic NRR by regulating organic ligands. The nitrogen fixation properties of the five synthesized Co-MOFs are better than those of Ni-MOFs. The results may be attributed to: Co²⁺ and Ni²⁺ with the same coordination configuration, the configurations of Co²⁺ and Ni²⁺ electrons in the orbitals are different, and the electronegativity of Co²⁺ is slightly lower than that of Ni²⁺. Fewer valence electrons in the d orbital and smaller electronegativity may be more likely to catalyze nitrogen reduction to ammonia synthesis.³⁴⁻³⁶

Five Co-MOFs with a similar composition and structure have different eNRR properties, mainly due to the following reasons: (1) Co-pds-H₂tdc based on the pds ligand (Fig. S20, ESI[†]) has a poor electrical conductivity due to the non-conjugation of the

pds ligand, therefore, Co-pds-H₂tdc has the worst nitrogen reduction performance of ammonia synthesis among the five Co-MOFs, which can be verified by the impedance results. (2) The other four ligands are all conjugated ligands, so the nitrogen reduction performance of the four Co-MOFs is better, in which the dpb ligand has a uniform distribution of electrons on the benzene ring, while bpat, bptz and dpt have a higher electron density on the heterocyclic ring. (3) When different heteroatoms are introduced into the organic ligand, the electronegativity difference between the elements regulates the charge density difference of the organic ligand,^{16,37} which can enhance the internal electric field and ultimately improve the performance of nitrogen reduction to synthesise ammonia. (4) In addition, the introduction of nitrogen and sulfur atoms in the bpat, bptz and dpt ligands can improve the electrical conductivity and regulate the adsorption capacity of the active sites. Heterogeneous atom doping is a feasible choice to increase the number of active sites, optimize the kinetic process, and regulate the electronic structure and adsorption free energy of the electrocatalyst, which was also confirmed by the results of the active specific surface area.^{38,39} (5) As an important nonmetallic element in nitrogen enzymes, sulfur plays a crucial role in the biological reduction of N₂.^{40,41} Many studies have shown that the introduction of sulfur atoms into a catalyst can promote the adsorption of N₂, and may change the charge distribution of metals and promote the hydrogenation of N₂ to NH₃.^{42,43} (6) By designing organic ligands with a similar structure and different functional blocks and constructing Co-MOFs with different pore environments, the pore structure can be adjusted to improve nitrogen adsorption and activation and ammonia desorption and increase ammonia yield. It can also balance the affinity and hydrophobicity of nitrogen, inhibit the hydrogen evolution reaction, and improve the Faraday efficiency.⁴⁴⁻⁴⁶

4. Conclusion

To summarize, five Co-MOFs with a similar structure for achieving enhanced nitrogen reduction reaction were developed. Owing to the enhanced electron transfer and increased electrochemical surface area, the Co-dpt-H₂tdc electrocatalyst exhibits the desirable catalytic activity for NH₃ production with a yield rate of 51.30 μg h⁻¹ mg_{cat}⁻¹ and a Faraday efficiency of 29.2%, which is significantly higher than those of other four Co-MOFs. This work provides insights into the field of optimizing ligands to improve the performance of nitrogen reduction electrocatalysts.

Author contributions

Ling Qin: methodology, conceptualization, supervision, writing – review and editing, project administration, and funding acquisition. Ying-Xin Zhao: writing – original draft, methodology, conceptualization, formal analysis, data curation, and validation. Qiang Liu: validation and data curation. Jin-Long

An: validation and data curation. Han-Xi Wang: validation and data curation. Mao-Feng Zhang: supervision. Cheng-Wu Shi: supervision. He-Gen Zheng: supervision.

Data availability

Crystallographic data for four Co-MOFs have been deposited at the CCDC under 2350963, 2350964, 2269367 and 2269368.

Conflicts of interest

There are no conflicts to declare.

Acknowledgements

This work was supported by grants from the National Natural Science Foundation of China (21601045, 62275072) and Anhui Provincial Key Research and Development Plan (2022i01020024).

References

- 1 H. A. Alhadidi Almheiri, N. Singh, D. Shetty, K. Polychronopoulou and A. A. Alhammadi, A Mo-salicylaldehyde-linker (Mo-Tp) based 2D MOF as a single-atom catalyst for the nitrogen reduction reaction, *J. Mater. Chem. A*, 2024, **12**, 7058–7066.
- 2 X. Y. Chen, Y. R. Wang and X. C. Meng, Fabrication of NiS_x/MoS₂ interface for accelerated charge transfer with greatly improved electrocatalytic activity in nitrogen reduction to produce ammonia, *Chem. Eng. J.*, 2024, **479**, 147701.
- 3 A. U. Shetty and R. Sankannavar, Exploring nitrogen reduction reaction mechanisms in electrocatalytic ammonia synthesis: A comprehensive review, *J. Energy Chem.*, 2024, **92**, 681–697.
- 4 H. M. He, H. K. Li, Q. Q. Zhu, C. P. Li, Z. Zhang and M. Du, Hydrophobicity modulation on a ferriporphyrin-based metal-organic framework for enhanced ambient electrocatalytic nitrogen fixation, *Appl. Catal., B*, 2022, **316**, 121673.
- 5 G. L. Gao, X. L. Chen, L. Han, G. Zhu, J. Jia, A. Cabot and Z. X. Sun, Advances in MOFs and their derivatives for non-noble metal electrocatalysts in water splitting, *Coord. Chem. Rev.*, 2024, **503**, 215639.
- 6 B. Han, L. X. Zhong, C. L. Chen, J. Ding, C. Lee, J. W. Liu, M. X. Chen, S. Tso, Y. Hu, C. D. Lv, Y. Han, B. Liu and Q. Y. Yan, Tuning Main Group Element-based Metal-Organic Framework to Boost Electrocatalytic Nitrogen Reduction Under Ambient Conditions, *Small*, 2023, **20**, 2307506.
- 7 Z. X. Li, B. Q. Yao, C. Q. Cheng, M. N. Song, Y. Qin, Y. Wan, J. Du, C. Y. Zheng, L. Y. Xiao, S. P. Li, P. F. Yin, J. Guo, Z. Q. Liu, M. T. Zhao and W. Huang, Versatile Structural Engineering of Metal-Organic Frameworks Enabling Switchable Catalytic Selectivity, *Adv. Mater.*, 2023, **36**, 2308427.
- 8 H. G. Zhang, H. Osgood, X. H. Xie, Y. Y. Shao and G. Wu, Engineering nanostructures of PGM-free oxygen-reduction catalysts using metal-organic frameworks, *Nano Energy*, 2017, **31**, 331–350.
- 9 N. Heidary, D. Chartrand, A. Guiet and N. Kornienko, Rational incorporation of defects within metal-organic frameworks generates highly active electrocatalytic sites, *Chem. Sci.*, 2021, **12**, 7324–7333.
- 10 C. Z. Liang, Q. M. Zhong, L. J. Pan, F. S. Liu, X. Li, J. W. Yang, Y. S. Ma, J. R. Zhou and S. T. Yang, Organic ligands regulate the environmental impacts of metal-organic frameworks on nitrogen-fixing bacterium Azotobacter vinelandii, *J. Hazard. Mater.*, 2023, **452**, 131373.
- 11 A. N. Singh, R. Anand, M. Zafari, M. Ha and K. S. Kim, Progress in Single/Multi Atoms and 2D-Nanomaterials for Electro/Photocatalytic Nitrogen Reduction: Experimental, Computational and Machine Learning Developments, *Adv. Energy Mater.*, 2024, 2304106.
- 12 L. Y. Wang, T. Li, X. T. Dong, M. B. Pang, S. T. Xiao and W. Zhang, Thiophene-based MOFs for iodine capture: Effect of pore structures and interaction mechanism, *Chem. Eng. J.*, 2021, **425**, 130578.
- 13 L. C. Chen, Y. T. Chen, X. W. Tu, S. X. Zhu, C. Sun, L. P. Zhang, W. H. Han, X. F. Duan, Q. Sun and H. Zheng, Fe/Zr-MOFs constructed by a sunlight-responsive ligand for efficient photocatalytic nitrogen fixation under ambient condition, *J. Colloid Interface Sci.*, 2023, **633**, 703–711.
- 14 Y. Peng, Y. Bai, C. L. Liu, S. Cao, Q. Q. Kong and H. Pang, Applications of metal-organic framework-derived N, P, S doped materials in electrochemical energy conversion and storage, *Coord. Chem. Rev.*, 2022, **466**, 214602.
- 15 T. Y. Wang, Z. Y. Guo, H. Oka, A. Kumatai, C. W. Liu and H. Li, Origin of electrocatalytic nitrogen reduction activity over transition metal disulfides: critical role of in situ generation of S vacancy, *J. Mater. Chem. A*, 2024, **12**, 8438–8446.
- 16 Y. T. Chen, Q. Sun, Z. G. Ni, X. W. Tu, C. Sun, S. X. Zhu, X. F. Duan, M. Jiang, Z.-J. Xie, M. Liu and H. Zheng, High-efficient solar-driven nitrogen fixation by modulating the internal electric-field of MOFs via n-site-enhanced charge density difference in organic ligands, *Chem. Eng. J.*, 2024, **482**, 148853.
- 17 C. P. Duan, Y. L. Ni, X. D. Yang, J. Y. Huang, Y. H. Shen, X. G. Gu, G. Ni, M. L. Ma, J. Li and L. Qin, Electrocatalytic hydrogen evolution of MOF derived materials based on conjugated or unconjugated ligands, *CrystEngComm*, 2024, **26**, 370–380.
- 18 R. Karthik and S. Natarajan, Interpenetrated and Catenated Zinc Thiosulfates Frameworks with dia and qtz Nets: Synthesis, Structure, and Properties, *Cryst. Growth Des.*, 2016, **16**, 2239–2248.
- 19 L. Qin, J. S. Hu, M. D. Zhang, Z. J. Guo and H. G. Zheng, Structure–property relationship of homochiral and achiral supramolecular isomers obtained by one-pot synthesis, *Chem. Commun.*, 2012, **48**, 10757–10759.
- 20 S. Tougaard, Practical guide to the use of backgrounds in quantitative XPS, *J. Vac. Sci. Technol., A*, 2021, **39**, 2304106.
- 21 H. T. Wang, W. Wang, M. Asif, Y. Yu, Z. G. Wang, J. L. Wang, H. F. Liu and J. W. Xiao, Cobalt ion-coordinated self-assembly

synthesis of nitrogen-doped ordered mesoporous carbon nanosheets for efficiently catalyzing oxygen reduction, *Nanoscale*, 2017, **9**, 15534–15541.

22 C. Y. Zhu, Y. Aoki and H. Habazaki, Co₉S₈ Nanoparticles Incorporated in Hierarchically Porous 3D Few-Layer Graphene-Like Carbon with S, N-Doping as Superior Electrocatalyst for Oxygen Reduction Reaction, *Part. Part. Syst. Charact.*, 2017, **34**, 1700296.

23 Q. Q. Ji, L. Bi, J. T. Zhang, H. J. Cao and X. S. Zhao, The role of oxygen vacancies of ABO₃ perovskite oxides in the oxygen reduction reaction, *Energy Environ. Sci.*, 2020, **13**, 1408–1428.

24 S. J. Luo, X. M. Li, W. G. Gao, H. Q. Zhang and M. Luo, An MOF-derived C@NiO@Ni electrocatalyst for N₂ conversion to NH₃ in alkaline electrolytes, *Sustainable Energy Fuels*, 2020, **4**, 164–170.

25 A. Maibam, I. B. Orhan, S. Krishnamurty, S. P. Russo and R. Babarao, Surface Electronic Properties-Driven Electrocatalytic Nitrogen Reduction on Metal-Conjugated Porphyrin 2D-MOFs, *ACS Appl. Mater.*, 2024, **16**, 8707–8716.

26 H. L. S. Santos, P. G. Corradini, M. Medina and L. H. Mascaro, Effect of copper addition on cobalt-molybdenum electrodeposited coatings for the hydrogen evolution reaction in alkaline medium, *Int. J. Hydrg. Energy.*, 2020, **45**, 33586–33597.

27 H. H. Zhang, S. H. Yan, W. Yi, X. Ma, J. He, Y. B. Lu, L. H. Yi and X. Z. Wang, Ambient N₂ Reduction to NH₃ Electrocatalyzed by ZIF-67-Derived Nitrogen-Doped Porous Carbon Supported Co₉S₈ Nanomaterials, *ACS Sustainable Chem. Eng.*, 2024, **12**, 2893–2899.

28 J. Duan, D. Shao, X. He, Y. Lu and W. Wang, Model MoS₂@ZIF-71 interface acts as a highly active and selective electrocatalyst for catalyzing ammonia synthesis, *Colloids Surf. A*, 2021, **619**, 126529.

29 P. J. Guo, F. X. Yin, J. Zhang, B. H. Chen, Z. Y. Ni, L. L. Shi, M. Y. Han, Z. M. Wu and G. R. Li, Crystal-Phase and Surface-Structure Engineering of Bi₂O₃ for Enhanced Electrochemical N₂ Fixation to NH₃, *ACS Appl. Mater. Interfaces*, 2024, **16**, 17540–17552.

30 H. M. He, Q. Q. Zhu, Y. Yan, H. W. Zhang, Z. Y. Han, H. Sun, J. Chen, C. P. Li, Z. Zhang and M. Du, Metal-organic framework supported Au nanoparticles with organosilicone coating for high-efficiency electrocatalytic N₂ reduction to NH₃, *Appl. Catal. B*, 2022, **302**, 121673.

31 S. Chen, H. Jang, J. Wang, Q. Qin, X. Liu and J. Cho, Bimetallic metal-organic framework-derived MoFe-PC microspheres for electrocatalytic ammonia synthesis under ambient conditions, *J. Mater. Chem. A*, 2020, **8**, 2099–2104.

32 M. Y. Cong, X. Y. Chen, K. Xia, X. Ding, L. L. Zhang, Y. Jin, Y. Gao and L. X. Zhang, Selective nitrogen reduction to ammonia on iron porphyrin-based single-site metal-organic frameworks, *J. Mater. Chem. A*, 2021, **9**, 4673–4678.

33 Y. H. Wu, X. D. Kong, Y. C. Su, J. K. Zhao, Y. L. Ma, T. Z. Ji, D. Wu, J. Y. Meng, Y. Liu, Z. G. Geng and J. Zeng, Thiol Ligand-Modified Au for Highly Efficient Electroreduction of Nitrate to Ammonia, *Precis. Chem.*, 2024, **3**, 112–119.

34 L. Q. Hu, Y. M. Guo, J. Chang, Y. P. Lu, X. J. Su, X. Y. Zhang, D. Geng, Y. M. Ren, T. Wei, H. X. Zhang and J. Feng, Increasing Mo⁵⁺ in M-doped La₂(MoO₄)₃ (M = Fe, Co, Ni, Cu, and Zn) toward efficient electrocatalytic nitrogen fixation, *J. Mater. Chem. A*, 2024, **12**, 15893–15901.

35 Z. Wei, Y. Feng and J. Ma, Co-doped graphene edge for enhanced N₂-to-NH₃ conversion, *J. Energy Chem.*, 2020, **48**, 322–327.

36 R. Zhang, L. Jiao, W. J. Yang, G. Wan and H. L. Jiang, Single-atom catalysts templated by metal-organic frameworks for electrochemical nitrogen reduction, *J. Mater. Chem. A*, 2019, **7**, 26371–26377.

37 L. L. Wen, K. Sun, X. S. Liu, W. J. Yang, L. Y. Li and H. L. Jiang, Electronic State and Microenvironment Modulation of Metal Nanoparticles Stabilized by MOFs for Boosting Electrocatalytic Nitrogen Reduction, *Adv. Mater.*, 2023, **35**, 2210669.

38 A. Hayat, Alamgir, L. G. Huang, Z. P. Wang, R. Ullah and S. L. He, One-pot in situ synthesis of an NS-ligand co-doped metal-organic framework for the enhanced adsorption-assisted photocatalytic decontamination of metronidazole, *RSC Adv.*, 2024, **14**, 10229–10243.

39 Z. W. Liu, Y. Wu, B. Y. Liu, S. C. Oh, W. Fan, Y. Qian and H. X. Xi, Tuning the adsorption and separation properties of noble gases and N₂ in CuBTC by ligand functionalization, *RSC Adv.*, 2016, **6**, 91093–91101.

40 J. Li, S. Y. Hu, Y. Li, X. B. Fan, F. B. Zhang, G. L. Zhang and W. C. Peng, Pyrrolic N anchored atomic Ni-N₃-C catalyst for highly effective electroreduction of CO₂ into CO, *Carbon*, 2023, **206**, 62–71.

41 A. M. Liu, M. F. Gao, Y. C. Gao, X. F. Ren, Y. A. Yang, Q. Y. Yang, Y. Q. Li, L. G. Gao, X. Y. Liang and T. L. Ma, DFT study of Ru/graphene as high-performance electrocatalyst for NRR, *Inorg. Chem. Commun.*, 2020, **120**, 108169.

42 J. Wang, S. Wang and J. P. Li, S-Doped three-dimensional graphene (S-3DG): a metal-free electrocatalyst for the electrochemical synthesis of ammonia under ambient conditions, *Dalton Trans.*, 2020, **49**, 2258–2263.

43 H. J. Wang, S. L. Liu, H. G. Zhang, S. L. Yin, Y. Xu, X. N. Li, Z. Q. Wang and L. Wang, Three-dimensional Pd-Ag-S porous nanosponges for electrocatalytic nitrogen reduction to ammonia, *Nanoscale*, 2020, **12**, 13507–13512.

44 P. Wang, K. Chen, Q. Liu, H. W. Wang, M. Azam, S. I. Al Resayes, Y. Lu and W. Y. Sun, Fine tuning of catalytic and sorption properties of metal-organic frameworks via in situ ligand exchange, *Dalton Trans.*, 2017, **46**, 11425–11430.

45 H. X. Deng, C. J. Doonan, H. Furukawa, R. B. Ferreira, J. Towne, C. B. Knobler, B. Wang and O. M. Yaghi, Multiple Functional Groups of Varying Ratios in Metal-Organic Frameworks, *Science*, 2010, **327**, 846–850.

46 D. Kim, H. Ha, Y. Kim, Y. Son, J. Choi, M. H. Park, Y. Kim, M. Yoon, H. Kim, D. Kim and M. Kim, Experimental, Structural, and Computational Investigation of Mixed Metal-Organic Frameworks from Regiosomeric Ligands for Porosity Control, *Cryst. Growth Des.*, 2020, **20**, 5338–5345.